

Electronic Supporting Information for:

Ultrafast nonradiative deactivation of photoexcited
8-oxo-hypoxanthine: a nonadiabatic molecular
dynamics study

Joanna Jankowska^{1} and Robert W. Góra^{2*}*

¹ Faculty of Chemistry, University of Warsaw, 02-093 Warsaw, Poland

² Department of Physical and Quantum Chemistry, Wrocław University of Science and
Technology, 50-370 Wrocław, Poland

Table S1. Active space (AS) orbitals for the XMS-CASPT2/cc-pVDZ calculations: (a.) the occupied, and (b.) the unoccupied orbitals in the closed-shell ground-state configuration.

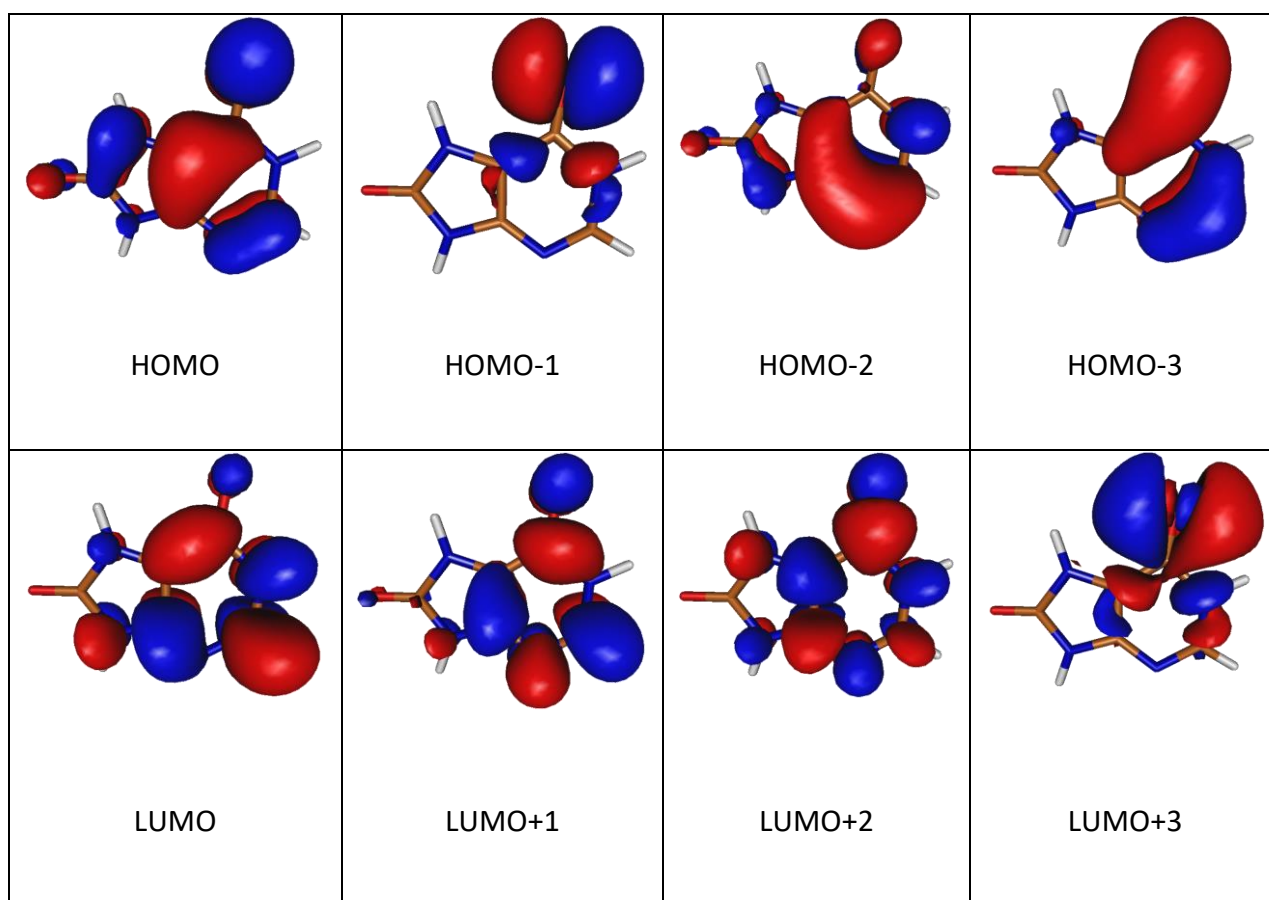
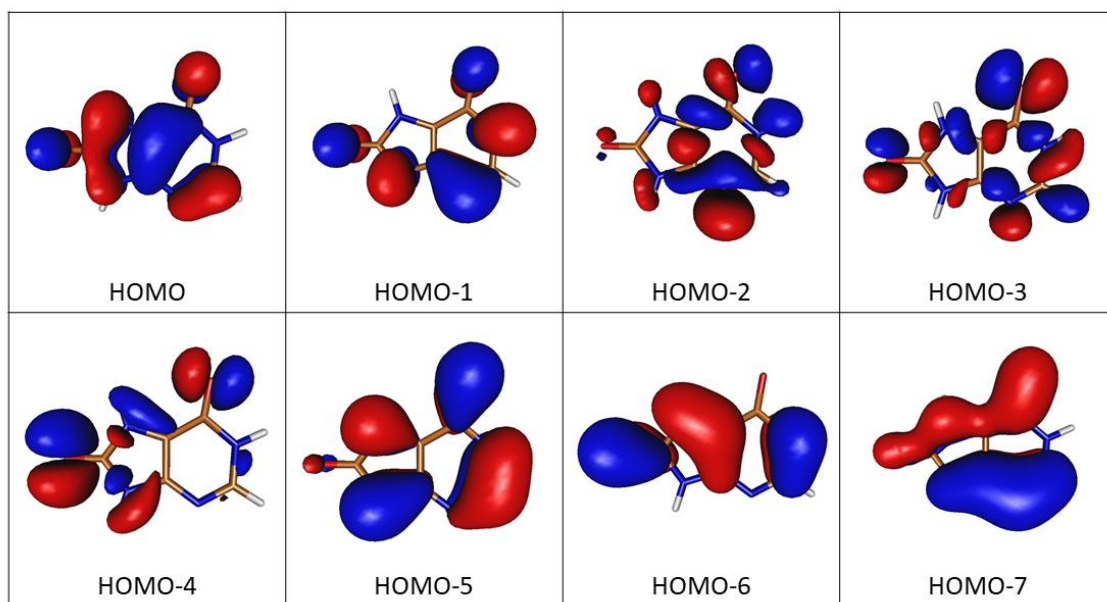


Table S2. Active space (AS) orbitals for the OM2/MRCI calculations: (a.) the occupied, and (b.) the unoccupied orbitals in the closed-shell ground-state configuration.

a.



b.

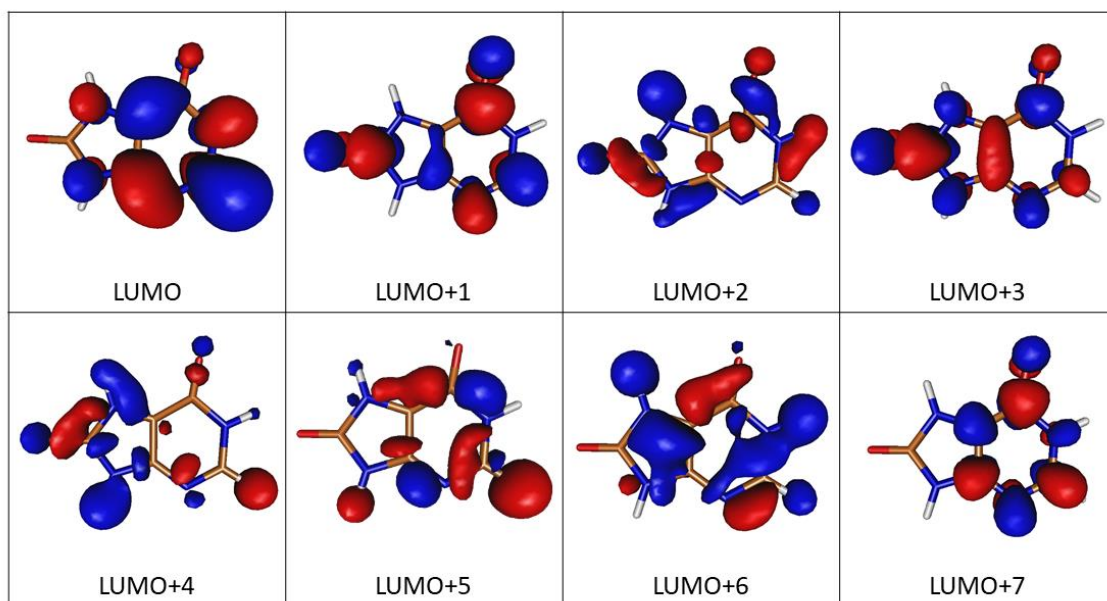


Table S3. Relative energies (in eV, corrected for the zero-point vibration energy (ZPE)) and optimized structures of the chemically relevant 8-oxo-hypoxanthine tautomers. For clarity, only the most stable rotamers have been presented. The geometries and ZPEs were calculated at the DFT(B2PLYP)/Def2-TZVP level, with energies recalculated at the CCSD(T)/Def2-TZVP level of theory on the DFT-optimize structures.

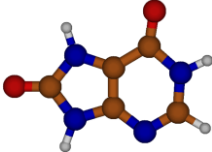
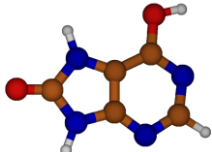
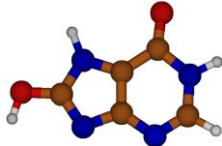
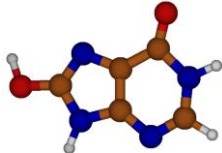
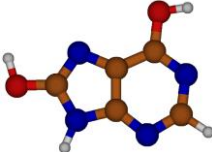
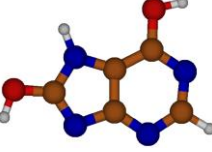
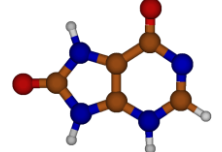
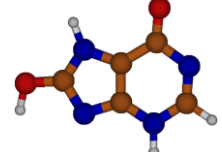
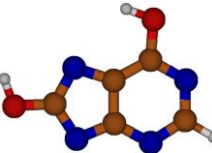
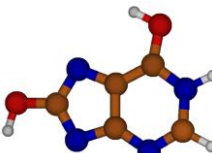
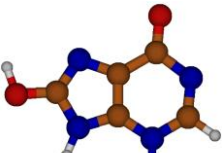
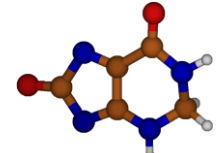
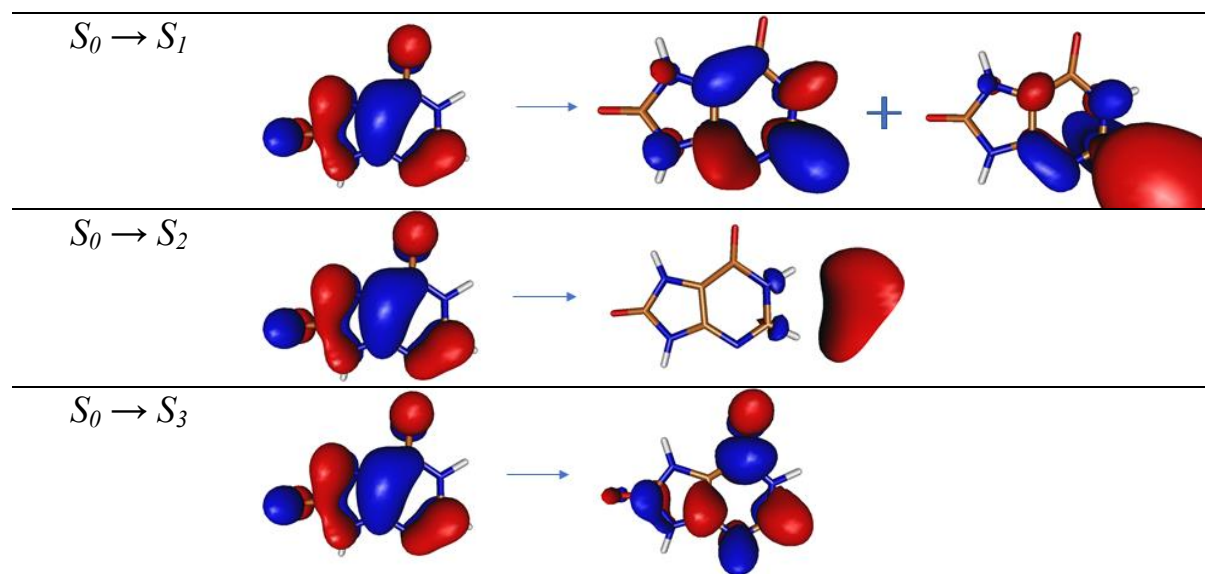
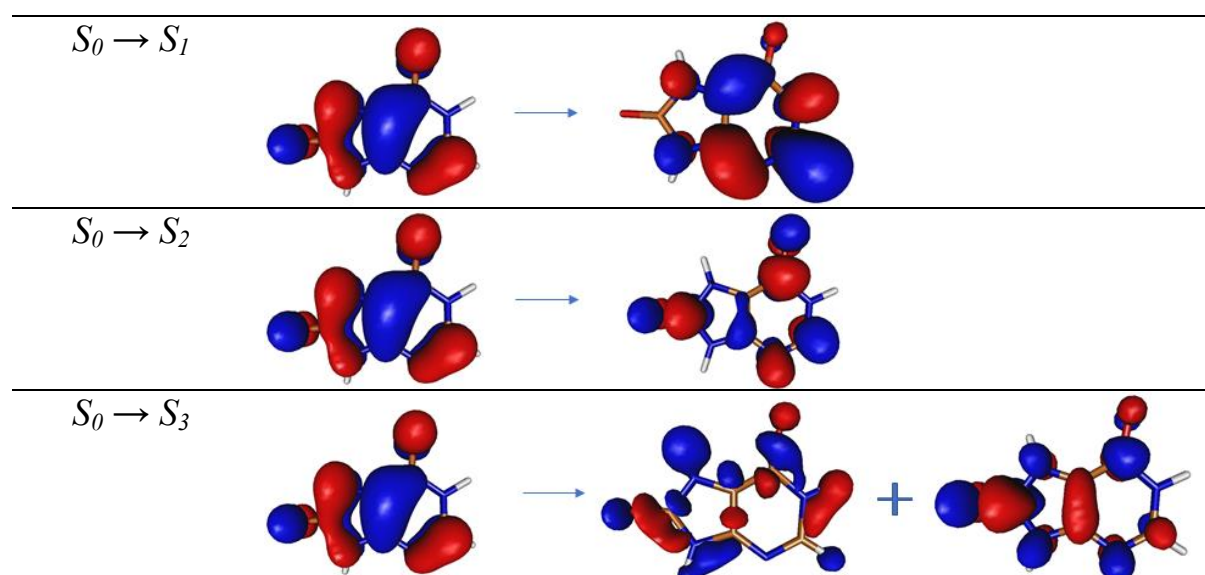
nh1-nh7-nh9 (keto, 0.000) 	oh6-nh7-nh9 (enol, 0.068) 	nh1-nh7-oh8 (0.432) 	nh1-oh8-nh9 (0.483) 
oh6-oh8-nh9 (0.555) 	oh6-nh7-oh8 (0.624) 	nh3-nh7-nh9 (0.724) 	nh3-nh7-oh8 (0.811) 
nh3-oh6-oh8 (0.938) 	nh1-oh6-oh8 (1.134) 	nh3-oh8-nh9 (1.327) 	nh1-ch2-nh3 (1.721) 

Table S4. The leading orbital contributions to lowest-energy electronic excitations at the (a) ADC(2)/aug-cc-pVDZ, (b) OM2/MRCI, (c) ADC(2)/aug-cc-pVTZ, and (d) XMS-CASPT2/cc-pVDZ levels of theory for the most stable di-keto form.

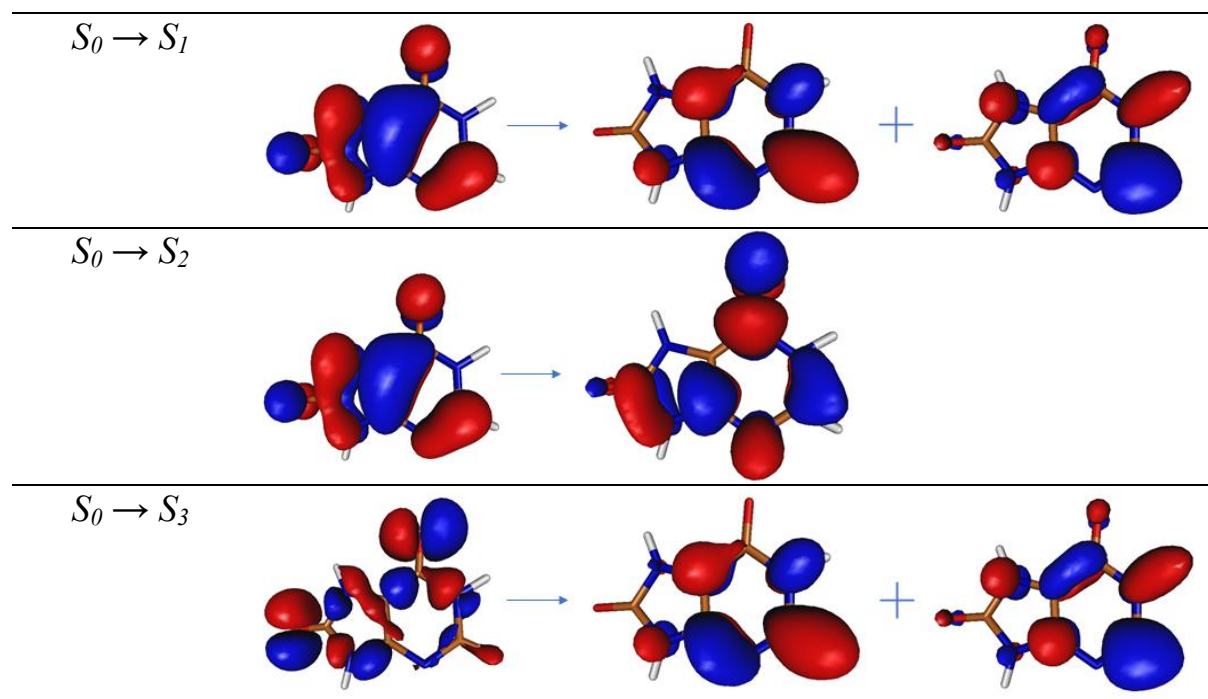
(a) ADC(2)/aug-cc-pVDZ



(b) OM2/MRCI



(c) ADC(2)/aug-cc-pVTZ



(d) XMS-CASPT2/cc-pVDZ

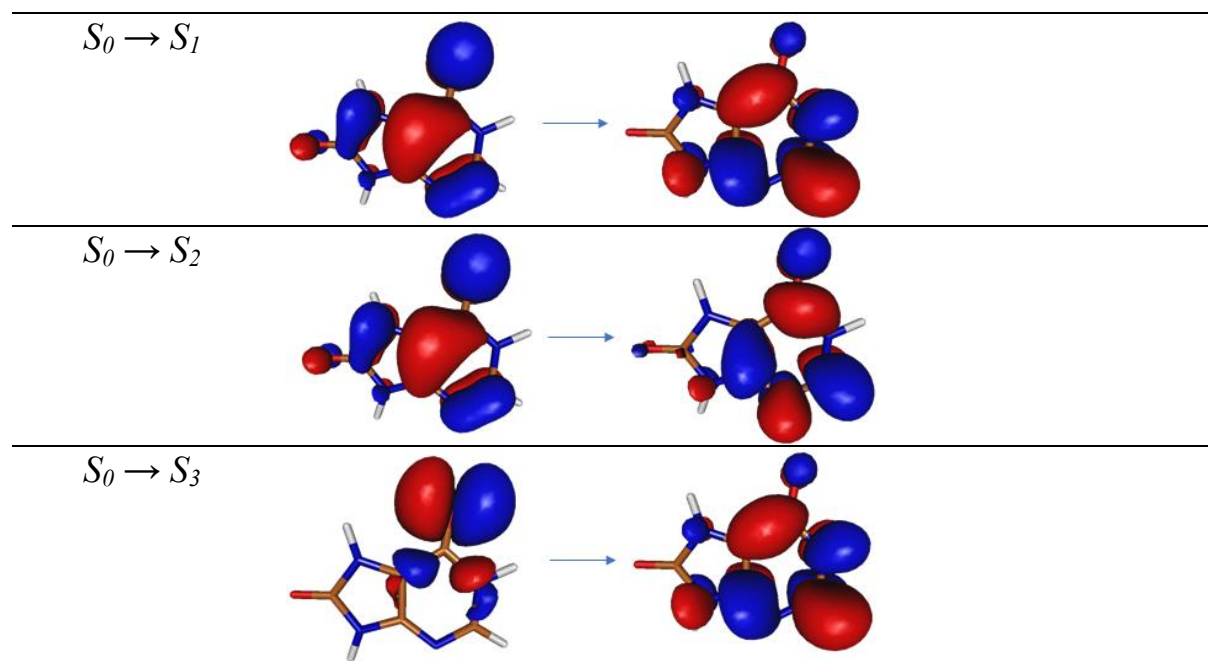


Table S5. Absorption spectrum of the lowest-energy enol form, calculated at the ADC(2)/aug-cc-pVDZ and ADC(2)/aug-cc-pVTZ levels of theory at the MP2/aug-cc-pVDZ geometry, with the leading orbital excitation contributions calculated at the ADC(2)/aug-cc-pVDZ level.

	<i>ADC(2)/aug-cc-pVDZ</i>			<i>ADC(2)/aug-cc-pVTZ</i>		
	E / eV	f. osc.	Character	E / eV	f. osc.	Character
S_1	4.84	0.1298	$\pi\pi^*$	4.81	0.1295	$\pi\pi^*$
S_2	5.28	0.1224	$\pi\pi^*$	5.26	0.1209	$\pi\pi^*$
S_3	5.31	0.0003	$\pi\sigma^*$	5.49	0.0013	$n\pi^*$
S_4	5.53	0.0009	$n\pi^*$	5.51	0.0004	$\pi\sigma^*$
S_5	5.60	0.0036	$n\pi^*$	5.55	0.0029	$n\pi^*$
S_6	6.03	0.0009	$\pi\sigma^*$	6.25	0.0008	$\pi\sigma^*$

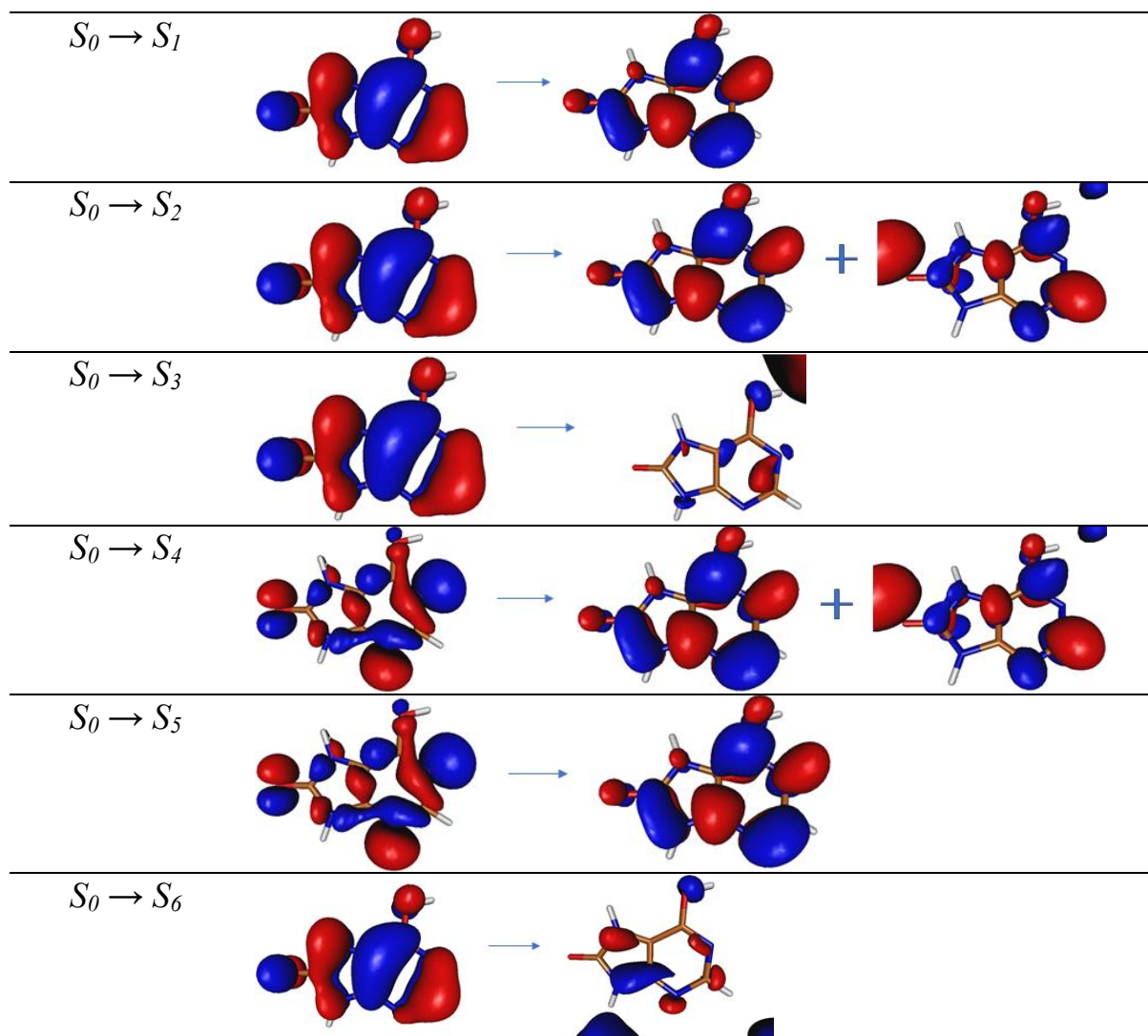
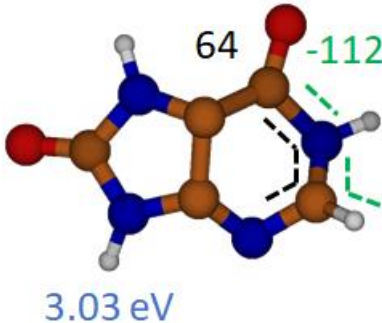
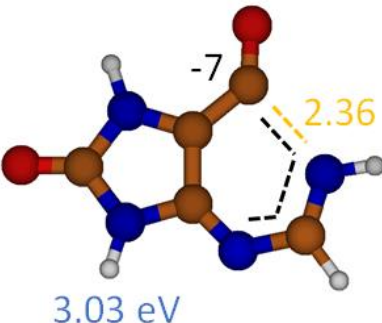
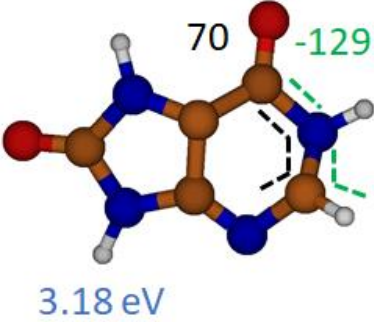
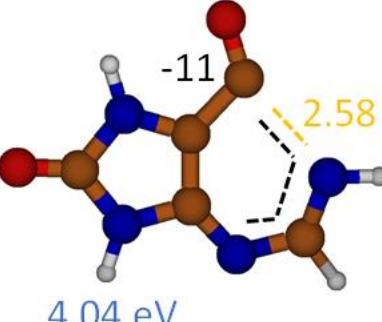
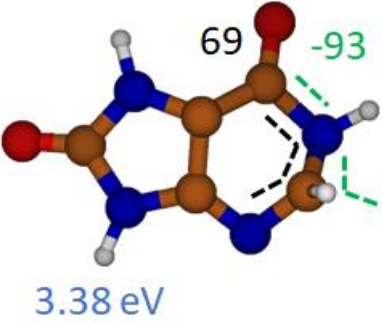
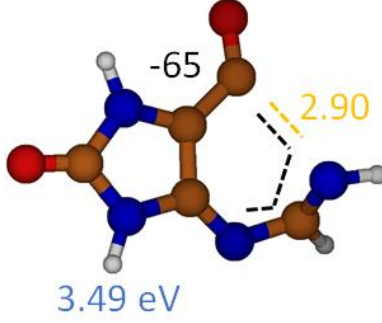


Table S6. Absorption spectrum of the lowest-energy keto form, calculated at the ADC(2)/aug-cc-pVDZ and ADC(2)/aug-cc-pVTZ levels of theory at the MP2/aug-cc-pVDZ geometry. The leading orbital excitation contributions can be found in Table S3.

	<i>ADC(2)/aug-cc-pVDZ</i>			<i>ADC(2)/aug-cc-pVTZ</i>		
	E / eV	f. osc.	Character	E / eV	f. osc.	Character
S_1	4.17	0.0935	$\pi\pi^*$	4.15	0.0932	$\pi\pi^*$
S_2	4.93	0.0003	$\pi\sigma^*$	4.92	0.2230	$\pi\pi^*$
S_3	4.95	0.2230	$\pi\pi^*$	4.97	0.0000	$n\pi^*$
S_4	5.00	0.0000	$n\pi^*$	5.13	0.0002	$\pi\sigma^*$
S_5	5.29	0.0005	$\pi\sigma^*$	5.50	0.0006	$\pi\sigma^*$
S_6	5.77	0.0000	$\pi\sigma^*$	5.54	0.0002	$n\pi^*$

Table S7. Optimized structures of MECP-RP and MECP-CN, determined at OM2/MRCI, MP2|ADC(2)/aug-cc-pVDZ, and XMS-CASPT2 levels of theory, with marked energies (in blue) and the most characteristic structural parameters: dihedral angles $C_6N_1C_2N_3$ (black), $C_6N_1C_2H$ (green), and C_6N_1 distance (yellow).

	MECP-RP	MECP-CN
OM2/MRCI		
MP2 ADC(2)/ aug-cc-pVDZ		
XMS-CASPT2/ cc-pVDZ		

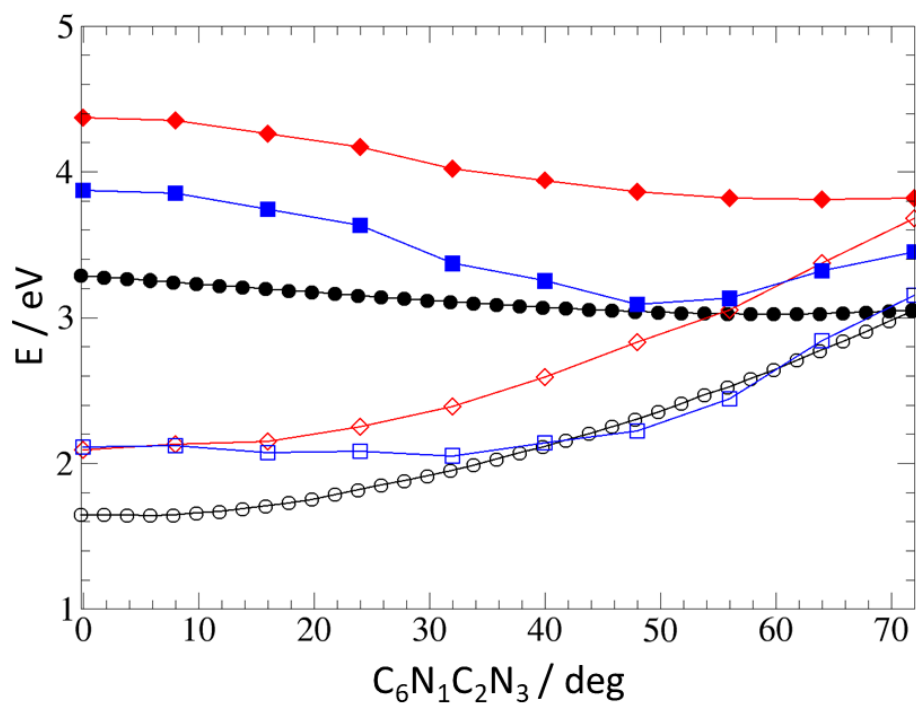


Figure S1. Single-point energy check along the adiabatic ring-puckering relaxation path obtained for state S_1 at the OM2/MRCI level of theory. The black circles, red diamonds, and blue squares correspond to results of the OM2/MRCI, ADC(2)/cc-pVDZ, and SF-ADC(2)/cc-pVDZ calculations, respectively, while full/empty symbols denote energy of S_1/S_0 states.

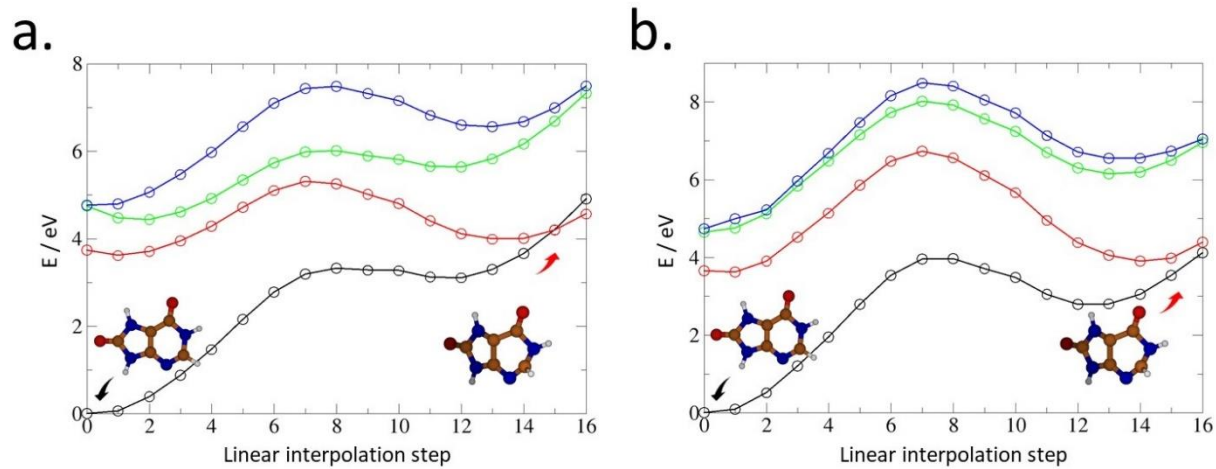


Figure S2. Linear-interpolation path between Franck-Condon and RP-MECP points for the keto-tautomer calculated at (a.) ADC(2)/aug-cc-pVDZ and (b.) OM2/MRCI levels of theory. The interpolation was performed in the internal-degree-of-freedom representation.

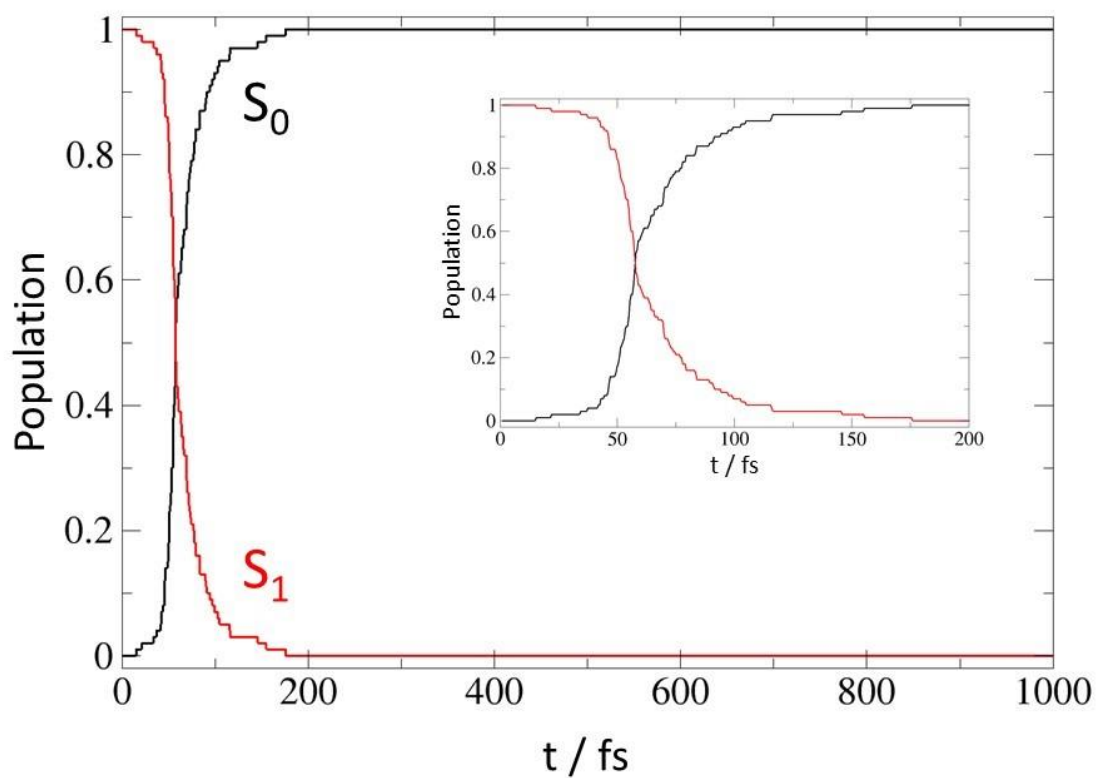


Figure S3. NAMD states population evolution obtained at the OM2/MRCI level of theory: S_0 – black, S_1 – red line, respectively. The inset focuses on the initial 200 fs of the relaxation dynamics.

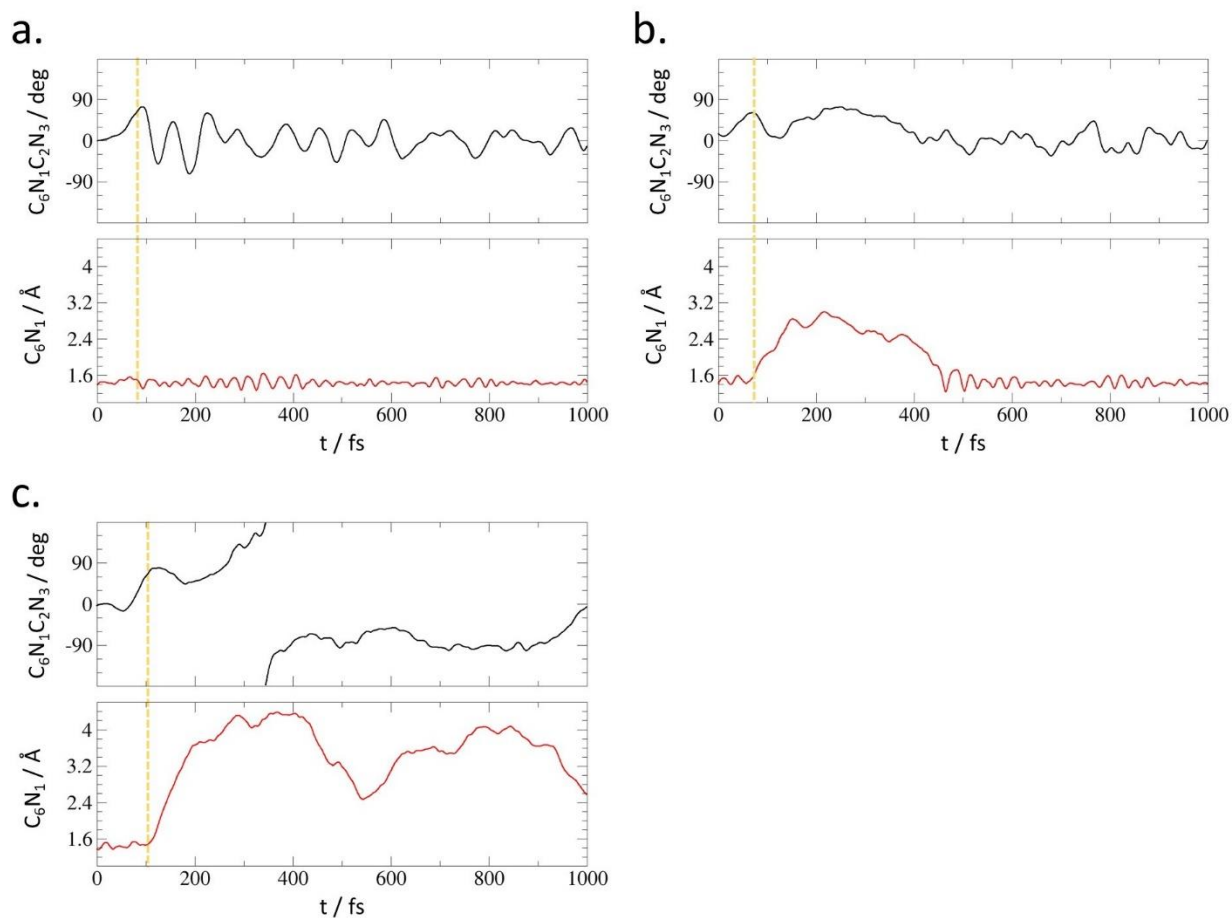


Figure S4. Evolution of the $C_6N_1C_2N_3$ and C_6N_1 coordinates along typical NAMD trajectories belonging to set I – closed forms produced with pure ring deformation (a.), set II a. – closed forms produced with ring deformation followed by the reversible C-N bond cleavage (b.), and set II b. – the final open isomers (c). The vertical lines mark the moment of the $S_1 \rightarrow S_0$ hopping; results calculated at the OM2/MRCI level of theory.

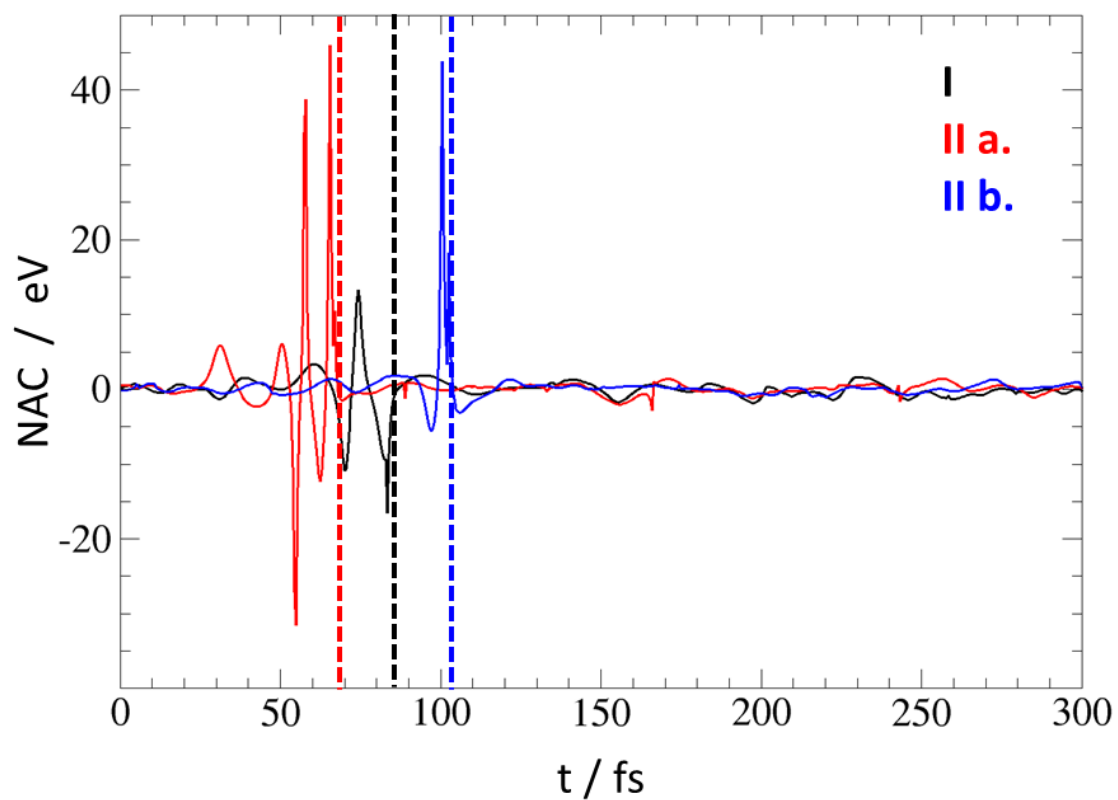


Figure S5. Nonadiabatic coupling (NAC) evolution for trajectories presented in Fig. S3, representing sets I, II a., and II b. The vertical dotted lines mark the moment of $S_1 \rightarrow S_0$ hopping.

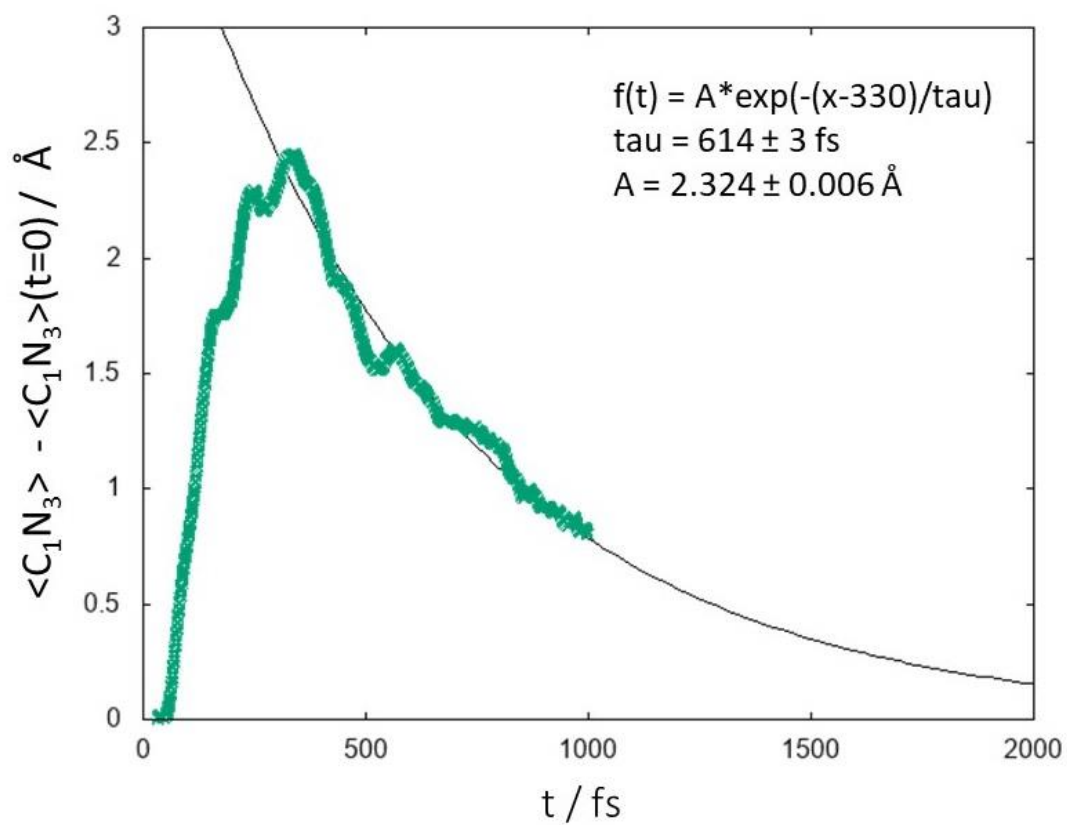


Figure S6. The open-ring isomer conversion dynamics to the closed-ring photoproduct with an exponential decay fit. The open-ring form population is quantified with deviation of the mean C-N bond length from its equilibrium value.

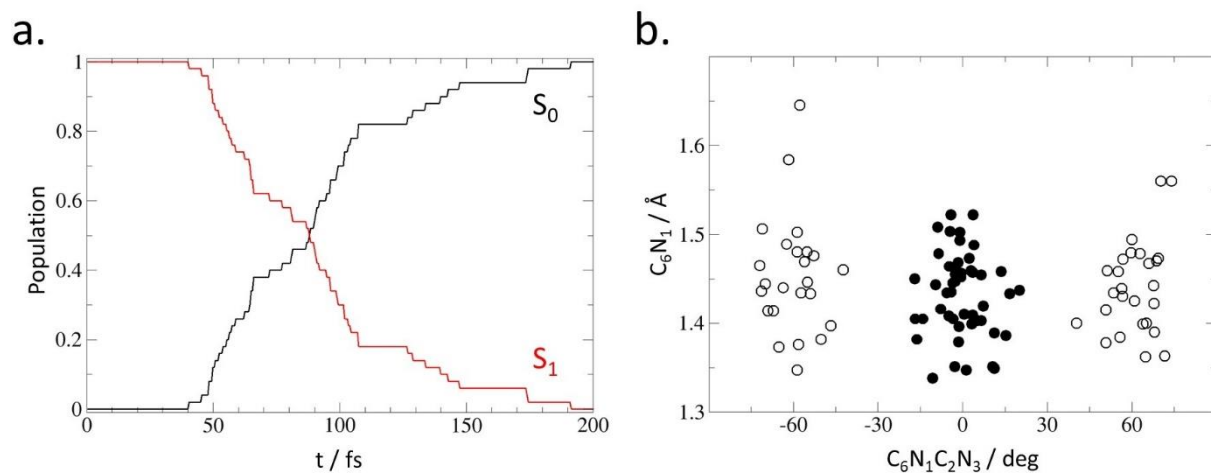


Figure S7. (a.) NAMD states population evolution: S_0 – black, S_1 – red line, respectively; (b.) Correlation graph showing distribution of starting (full circles) and hopping (empty circles) points with respect to the $C_1N_3-C_1N_3C_5N_7$ coordinates; results calculated at the ADC(2)/aug-cc-pVDZ level of theory.